Influence of powder type and binder saturation on binder jet 3D–printed and sintered Inconel 625 samples

Runbo Jiang [1,2] · Lorenzo Monteil [1] · Katerina Kimes [1] · Amir Mostafaei [3] · Markus Chmielus [1]

Abstract

Binder jet 3D printing combined with post-deposition sintering is a non-beam additive manufacturing (AM) method for the creation of complex 3-dimensional structures. Binder saturation and particle morphology are two important factors affecting the quality of printed parts. Here, we investigated the effects of binder saturation on dimension accuracy, porosity, microstructure, and microhardness of nickel-based alloy 625 samples made of differently atomized powders. Argon gas atomized (GA) and water atomized (WA) nickel-based alloy 625 powders were used to binder jet samples for a detailed comparative study. The optimal binder saturation for WA system is 60 to 70%, whereas for GA system the optimal is about 80%. Generally, GA samples achieved better overall quality than WA samples in terms of packing density, dimensional accuracy, sintered density, and microhardness. This difference is attributed mainly to the particle morphology including sphericity and roundness. The critical threshold for visible binder bleeding phenomenon in WA and GA systems is determined to be 120% and 140% binder saturation, respectively. Mechanisms for binder bleeding phenomenon at different saturation levels for WA and GA systems are discussed in detail. A pore evolution model is proposed to better understand the printing and sintering processes.

1 Introduction

Inconel Alloy 625 is a nickel-based superalloy that possesses high strength and resistance to elevated temperatures. It also demonstrates remarkable protection against corrosion and oxidation. Therefore, Inconel 625 is highly attractive for aerospace applications and in energy industries [1–3], and has stimulated extensive research interests.

Binder jet 3D printing (BJP) [1, 4], electron beam melting (EBM) [5], and laser beam melting (LPBF) [6], as emerging manufacturing methods in the field of additive manufacturing (AM), have been widely utilized to fabricate metallic structure

components. These AM technologies allow for the manufacturing of complex parts with considerable flexibility in geometry without the aid of tools and molds. BJP as one of the nonbeam-based AM methods deposits powder in a layer-by-layer fashion and selectively joins powder particles in each layer with binder, which consists of polymers and solvent. The combination of fast, low-cost manufacturing; stress-free structures with complex internal and external geometries; isotropic properties of the final printed parts; and potential for very low surface roughness and high resolution is unique in AM and promises broad application potential.

A schematic binder jetting system is shown in Fig. 1, based on an ExOne Innovent system. During the BJP process, a hopper moves over the print bed and deposits powder, which is then spread evenly by a roller, rotating opposite the direction of motion, on the powder bed in a layer-by-layer fashion. A printhead moves over the powder bed and selectively deposits liquid binder on the surface which migrates within and between layers, gluing the powder particles together to form 2D high-resolution layers of the 3D part. At the end of each layer printing, a heat lamp moves over and provides in-process drying to ensure sufficient binder drying for subsequent recoating and printing of the following layers. The build

✉ Markus Chmielus
chmielus@pitt.edu

1 Department of Mechanical Engineering and Materials Science, University of Pittsburgh, Pittsburgh, PA 15261, USA

2 Present address: Department of Materials Science and Engineering, Carnegie Mellon University, Pittsburgh, PA 15213, USA

3 Department of Mechanical, Materials and Aerospace Engineering, Illinois Institute of Technology, 10 W 32nd Street, Chicago, IL 60616, USA

Fig. 1 Schematic illustration of the ExOne Innovent binder jet 3D printer with the printing directions specified by the red arrows (not drawn to scale)
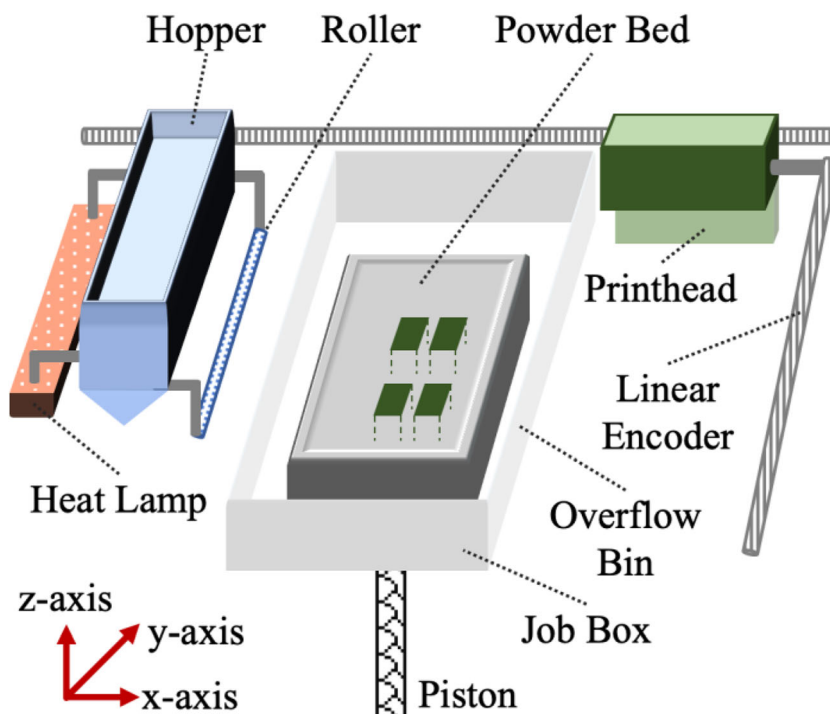

platform is then lowered by the distance of one-layer thickness. This process is repeated until the 3D object is finalized within the powder bed. In the curing step, the printed green parts along with the job box are heat treated at about 180 °C to cure the binder, leaving pendular bonds. Then, unbounded powder is brushed off the bounded parts and recycled. The 3D object at this point is called a "green part" and consists of metal powder held together by a crosslinked binder. The green parts are then sintered to form a densified component or infiltrated to create a composite.

The powder-binder interaction is largely determined by the properties of the binder material and feedstock powder. Powder with spherical morphology has better flowability and packing density [7]. When irregular powder with low flowability is spread, lower powder bed density is expected due to interparticle friction and a looser arrangement of powder particles. In the BJP AM process, the binder saturation level is an important factor that must be tailored carefully

[8–18]. Binder saturation is defined as the ratio of the volume of deposited binder (V_{Binder}) to the volume of open voids in the powder bed (V_{Voids}) [4]. If the saturation level is much higher than the optimal saturation, the excess liquid binder tends to drift out of the intended boundaries of the printed geometry laterally or downward into the surrounding powder [10, 16, 19, 20], as shown in Fig. 2. Specifically, binder saturation over 100% means that the volume of binder injected would exceed the volume of voids in the powder bed for an optimum powder that can be used to accommodate liquid binder [21]. In this case, binder would permeate into the surrounding areas outside the desired printed shape, causing surfaces of a part migrating outwards and weakening feature sharpness. This migration phenomenon, called "bleeding," is a macroscopic flow of binder in the droplike features at high saturation that usually hang off at the bottom of a part [22]. On the other hand, if the amount of binder is not enough to effectively glue the powder and layers, the green part would not

Fig. 2 Photograph of the common BJP AM in-process defects from binder saturation: from left to right insufficient saturation, adequate saturation, and excessive saturation. The digital model for all three samples is designed to be a 10 × 10 × 10 mm cube
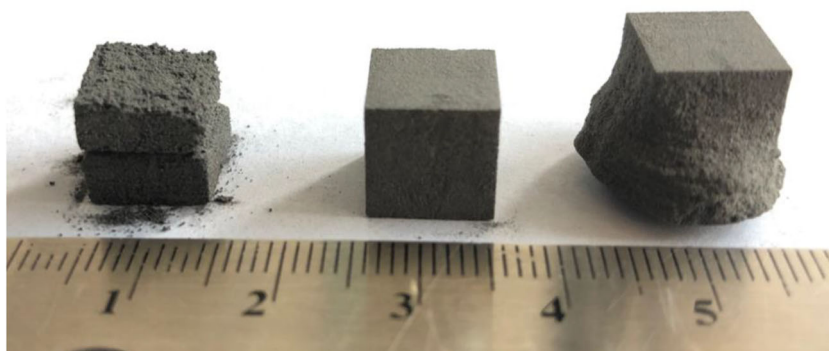
have sufficient mechanical strength to hold itself as a solid component, which results in weak bonding between the powder particles and between successive layers.

In this study, the effect of binder saturation levels on two differently atomized Inconel 625 powders is quantitated to determine the relationship between the binder deposited and the resulting green densities and densities, dimensional, and mechanical properties of sintered samples. The scientific insight and analysis obtained can be used to tailor the processing parameters and improve the reliability of the properties of final BJP Inconel 625 alloy parts depending on the specific applications. This is especially applicable to less used but usually cheaper WA powder for applications that do not require full density such as filtration. These findings may be transferred to other metal powders with similar characteristics.

2 Experimental procedures

The argon gas atomized and water atomized alloy 625 powders were obtained from Carpenter Technology Corporation and HAI Advanced Material Specialists, Inc., respectively. The manufacturer-certified chemical compositions provided in the powder material data sheet are given in Table 1. The powder morphology (sphericity and roundness) was characterized via ImageJ [23] of micrographs taken with an FEI Apreo scanning electron microscope. The particle size distribution was analyzed by Microtrac S3500 tri-laser diffraction particle analyzer using spherical and non-spherical particle algorithms.

An ExOne Innovent binder jet printer was used to manufacture parts. Figure 1 shows the schematic of the design used during printing as well as the representative cube samples. In this study, a total of 10 coupons with dimension of $10 \times 10 \times 10$ mm^3 were built using with the BA005 aqueous binder (ExOne), and default parameters: droplet size 80 pL, drying time 21 s, layer thickness of 100 μm, hopper oscillation speed 2500 rpm, recoat speed 90 rpm, roller traverse speed 30 mm/s, and roller rotation speed 600 rpm. In order to determine the influence of binder saturation, the saturation levels were set to be 50%, 60% (default), 70%, 80%, 100%, 120%, and 140%, respectively. The as-printed green parts were cured at 180 °C for 8 h (Yamato DX402C Drying Oven) and then sintered in a tube furnace (Across International TF1400) in an alumina powder bed with continuously pumped vacuum

atmosphere to evacuate any debinding products using the following thermal profiles: heating with 5 °C/min from room temperature to 600 °C, holding for 45 min, heating with 3.2 °C/min to 1000 °C, and further heating with 2.8 °C/min to the holding temperature (1270 °C for WA samples, 1285 °C for GA samples), holding for 4 h, and then cooling with 1 °C/min to 1200 °C, 3.1 °C/min to 500 °C and finally furnace cooling to room temperature [1]. Five samples for each combination of binder saturation and powder type were prepared. This sintering profile is composed of two primary stages: debinding and sintering. A 45-min hold occurred at 600 °C to burn the binder off and decrease the residue of carbon in printed parts. A 4-h sintering step occurred at 1270 °C for WA parts and at 1285 °C for GA parts to densify parts, as detailed in Ref. [1]

The densification of IN625 was evaluated by comparing powder bed packing density, green density, and final sintered density. Density measurement cup tests were conducted to directly measure the packing density of the powder bed according to [24]. Density measurement cups with inner vacant volumes of $5 \times 5 \times 10$ mm^3, $10 \times 10 \times 10$ mm^3, $20 \times 20 \times 10$ mm^3, and $40 \times 40 \times 10$ mm^3 were prepared in order to verify size dependency of the measurement. Dimensional accuracy and green density of as-printed parts were measured with a Mitutoyo caliper (0.01 mm resolution) and OHAUS AX324 precision balance (0.1 mg resolution) according to [13]. The inner dimension of cups in the CAD file was used to calculate volume. Density of the sintered samples was measured via the Archimedes principle (AP) with OHAUS density determination kit. To examine the microstructural features of the sintered parts, cross-sections were cut from the specimens using a low-speed diamond saw (Allied TechCut 4). The sectioned surfaces were then mounted, ground (320 grit SiC grinding paper), and polished (using first 9 μm, then 3 μm DiaPro water-based diamond suspension, and then OP-S NonDry colloidal silica suspension) using a Struers Tegramin-25 automatic system. Microstructural characterizations were conducted with a FEI Apreo SEM equipped with a backscattered electron (BSE) detector. Density of the sintered samples was also determined from cross-sectional high-magnification optical micrographs (OM, pixel resolution < 1 μm) stitched together for the entire cross-sectional area and analyzed with ImageJ [23]. To determine the relative density, each obtained density was divided by the theoretical density of IN625 alloy, i.e., 8.44 g/cm^3 at room temperature.

Table 1 The as-provided composition and EDS composition of WA and GA Inconel 625 powders in [wt.%]

Element	Ni	Fe	Cr	Nb	Mo	Ti	Al	Co	Mn	Si
WA (provided)	Bal.	3.6	21.8	3.5	9.3	<0.4	<0.4	<1.0	0.4	--
WA (EDS)	Bal.	3.2	18.4	1.1	6.8	0.34	0	0.53	0.58	1.45
GA (provided)	Bal.	4.2	21.5	3.3	8.9	--	--	--	0.4	0.4
GA (EDS)	Bal.	2.5	23.9	1.9	6.5	0.27	0.04	0.37	0.54	0.03

Vickers microhardness tests were performed on the cross-sections of all samples using a LECO LM800 hardness tester with a load of 100 gf and a dwell time of 10 s. Hardness values were averaged from 10 indents of each sample.

3 Results and discussion

3.1 Powder characteristics and packing behaviors

The secondary electron micrographs of plan-view and cross-section of powder particles are shown in Fig. 3 along with powder size distribution, roundness, and sphericity of the feedstock IN625 WA and GA powders. The WA powder exhibited an extremely irregular morphology and rough surface, typical after the water atomization process. Internal pores are frequently observed in the cross-sections of WA powder in Fig. 3a. The GA powder has a more spherical morphology with minimal internal pores (Fig. 3b). The internal porosity in powder particles can be inherited by the sintered components [25]. A more comprehensive analysis for these two types of powders can be found in Ref. [26]. Another difference between WA and GA power is that WA powder shows a rather large distribution of particle sizes, ranging from 1.2 up to 176 μm. Roundness (Fig. 3d) and sphericity (Fig. 3e) are measured using scattered particle SEM images and ImageJ

software [23]. Flowability and wettability vary with surface roughness, and, thus, particle size, sphericity, and roundness as observed in [7, 21, 24]. The closer the roundness and sphericity values are to 1, the closer the particle morphology is to a smooth sphere [27]. As can be seen in Fig. 3e, the larger a WA powder particle, the more likely for it to be more irregularly elongated shaped (lower sphericity). The widespread data of WA powder in both roundness and sphericity corresponds to its wide particle size distribution. Therefore, it is implied that the flowability and binder wettability of WA powder are lower than GA powder [28].

The powder packing densities were determined to be 3.75 ± 0.10, 3.83 ± 0.06, and 3.85 ± 0.03 g/cm^3 for WA powder and 4.81 ± 0.13, 4.79 ± 0.04, and 4.81 ± 0.01 g/cm^3 for GA powder, respectively, depending on inner volume cup size (as shown in Fig. 4). Within the scope of this study, powder bed density was found to increase for WA powder with the inner volume of the measurement cups as the effect of the weight of the powder hanging on the cup wall becomes less significant in the cups with larger volume. Additionally, freely settled powder loose density is determined to be 3.43 g/cm^3 and 4.28 g/cm^3 for WA and GA powder, respectively. In summary, in our study the irregularly shaped WA powder exhibited 20–22% lower packing and apparent densities than the GA powder which are directly related to the green part density.
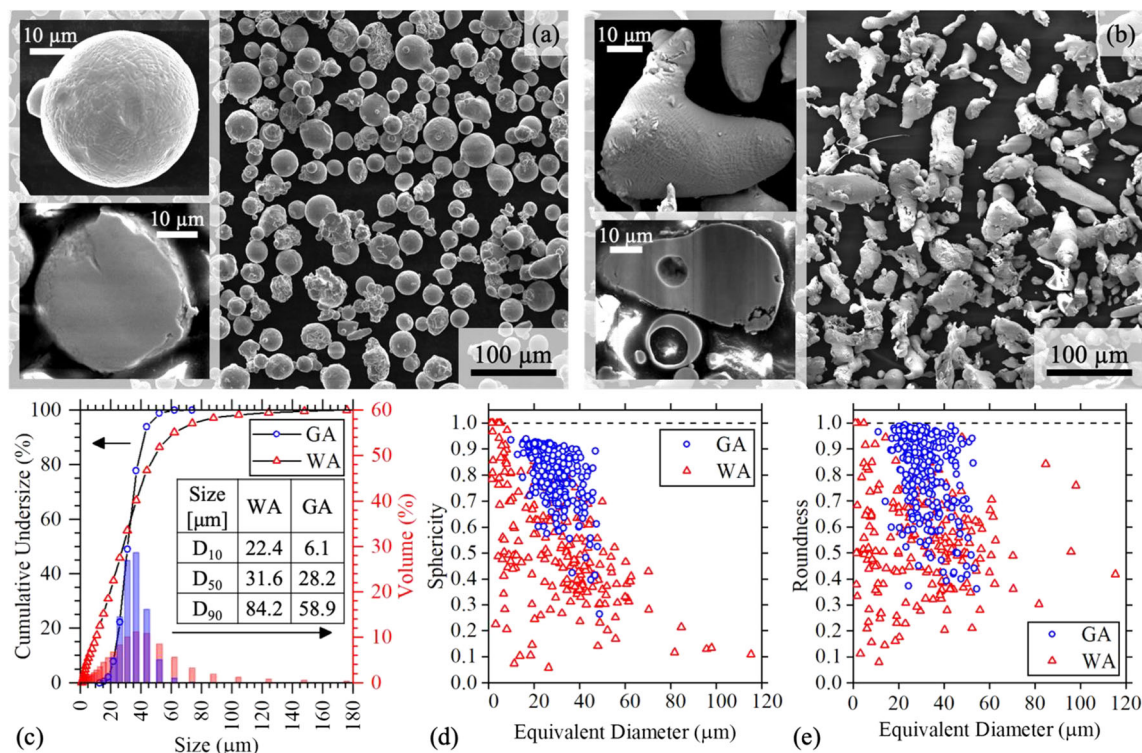

Fig. 3 Secondary electron SEM micrographs for IN625 powders: (a) GA powder and (b) WA powder, cross-sectional micrographs taken from the (a) GA and (b) WA powders showing pores inside the powders; (c) particle size distribution from the GA and WA powders; particle morphology analysis of the (d) roundness and (e) sphericity of GA and WA powders
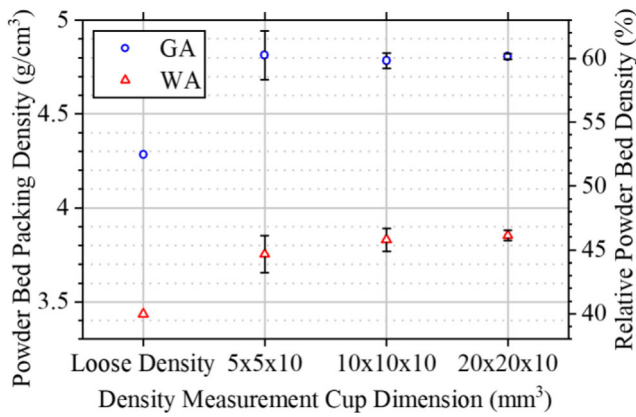
Fig. 4 Powder bed packing density of the GA and WA IN625 alloy as measured in the density measurement cups

3.2 Green density and dimensional accuracy

Figure 5 presents the variation of green density of GA and WA IN625 samples printed at different binder saturation levels. Prior to the sintering step, the green part density of GA samples is, as expected, higher than that of WA IN625. The difference in green density between WA and GA samples is caused by the difference in particle packing behaviors during powder spreading, as shown in Fig. 4, which shows that the packing rate of WA powder is approximately 20–22% lower than the packing rate of GA powder. It follows that the overall green densities of the parts also have a difference of around 23–31% (Fig. 5). The difference in powder packing rate can be explained by the difference in morphology of the GA and WA powder. It is known that spheres pack more efficiently than irregular particles. Therefore, the spherical GA powder spreads more densely than the irregular WA powder. In addition, for GA powder, saturation levels of 80% and 100% result in higher green part density, which are 51.8% and 51.9%, respectively, while for WA powder, saturation levels
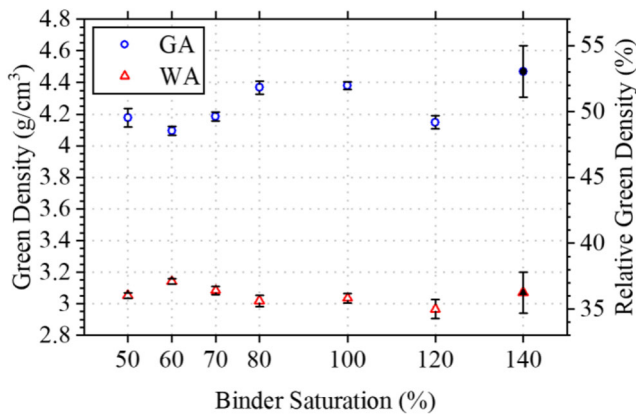
of 60% and 70% result in higher green density: about 37.2% and 36.5%, respectively. Therefore, in terms of obtaining higher green part density, binder saturation higher than the default value (60%) is strongly recommended for GA powder, and binder saturation around the default value is best for WA powder. Note that the green density values of both GA and WA sample at 140% binder saturation are marked as black data points, indicating these two values are not precise due to very large errors in the part volume measurements when extensive binder bleeding occurs.

Figure 6 presents the results of the linear dimensional accuracy of green parts made from (a) GA and (b) WA IN625 alloy. The nominal dimensional error, 0, corresponding to precisely 10 mm as designed in the digital CAD file, is marked as dashed black line in Fig. 4. For the binder jet–printed GA and WA IN625 samples, the mean dimensional errors in all three directions are always larger than zero, revealing that the caliper-measured green part dimensions are larger than those in the digital model. This pattern is true independent of the level of binder saturation, even when the saturation is less than the default value. In spite of this regularity, anisotropy in linear dimensional accuracy contingent on the directions was observed in both sets of samples. Two cases are observed, one when binder saturation does not cause bleeding, and another when the bleeding occurs. For WA samples, bleeding occurs at BS = 120% and 140%, and for GA samples, bleeding occurs at BS = 140%. In the first case, where there is no binder bleeding, with the exception of 70% and 100% gas atomized samples, there is generally a higher dimensional accuracy in the z-direction than in the x- and y-directions but differences are insignificant. Because saturation levels are appropriate in these cases for the amount of powder and the dry time, binder is fully absorbed and dried in each layer. As a result, the binder neither penetrates previous layers causing pools at the bottom nor bleeds out the sides. In the second case noted by binder bleeding, the x-direction and y-direction have higher mean errors and standard deviation values while the highest linear dimensional accuracy is found along the build direction (z-direction). Note that the differences in z-direction came from the base of the sample, not the top, as the roller produces a very smooth and dimensionally accurate surface. This phenomenon is thought to be caused by the different binder and powder bed interactions, including the binder spreading rate (i.e., lateral migration in the x- and y-directions) and penetration rate (vertical migration in the z-direction) [12]. In the present study, the liquid binder penetration rate in the lateral directions is higher than that in the vertical direction for samples where bleeding is observed. Though the x- and y-directions showed better dimensional accuracy, the mean error in the x-direction is slightly higher than that in y-direction for most cases. This indicates the extent of binder bleeding taking place in the printed head direction of motion (y-direction) is mitigated to a small extent.

Fig. 5 Green part density of Inconel 625 samples of GA and WA Inconel 625 printed with different binder saturation levels. Note that green density values for 140% binder saturation, which are marked as black data points, are not accurate due to the inaccurate measurement of volume caused by extensive binder bleeding

Fig. 6 Linear dimensional error of green parts fabricated from the (top) GA and (bottom) WA Inconel 625 alloy powders with various binder saturation levels
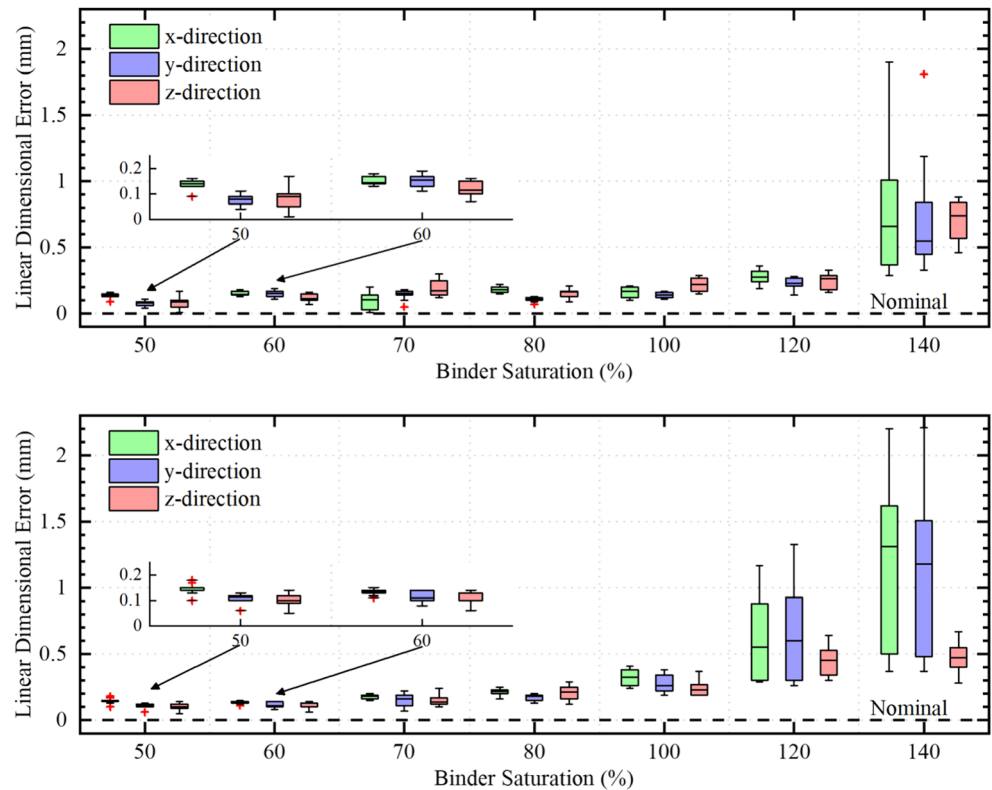
According to Fig. 6, the increase in binder saturation level increased the dimensional error and decreased the dimensional accuracy in all directions progressively and substantially. For example, the mean error value in x-direction increased substantially from 0.15 ± 0.02 mm to 1.17 ± 0.67 mm for WA IN625, and from 0.13 ± 0.03 mm to 0.77 ± 0.50 mm for GA IN625 powder from binder saturation 50% to 140%. The increase in binder saturation above 100% for WA and above 120% for GA significantly reduced the dimensional accuracy of green parts in all direction, especially in x- and y-directions. As can be seen in the Supplemental Fig. 11, the bleeding phenomenon is self-evident on the four side surfaces showing rugged texture when the saturation level is 120% and 140% for WA powder and 140% for GA powder. This also indicates that bleeding occurs for WA powder at a lower saturation levels than GA powder. This can be attributed to the different bleeding mechanisms, which will be discussed in Section 3.5. Therefore, in terms of obtaining better dimensional accuracy of green parts, binder saturation less than 100% is suitable for WA powder and saturation less than 120% is suitable for GA powder.

3.3 Sintered density measurements

Figure 7 shows the densification curves of GA and WA sintered samples, which were analyzed from optical micrographs taken from sectioned samples using ImageJ and Archimedes method measurements taken from the whole

sample. The density of GA samples is always higher than that of WA samples, regardless of the binder saturation levels, which is consistent with the green and packing densities of both powders. As the particle sizes and size distributions were very similar for WA and GA IN625 powders, as shown in Fig. 3, this higher sintered density in GA and lower density in WA sample are, therefore, caused by the difference in green density and particle morphology, pore evolution, and sintering mechanisms, which will be discussed in Section 3.4.
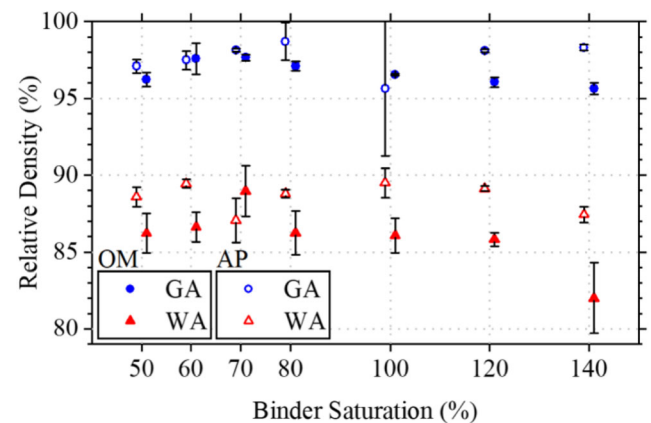

Fig. 7 Relative density measured from image analysis of optical micrographs (solid data points) and Archimedes method (hollow data points) of the sintered Inconel 625 samples printed with different binder saturation levels. Data points of binder saturation are staggered for better comprehensibility

WA samples printed with 60% binder saturation reached a maximum relative density of nearly 90%, while GA samples with 80% binder saturation achieved relative density >99%. For GA samples between 50 and 80% binder saturation levels, the sintered density increases with increasing saturation, and decreases when the saturation level exceeds 100%. For WA samples, the sintered relative density increases with increasing saturation between 50 and 60%, and decreases after the saturation goes beyond 70%. A similar trend was seen in the Archimedes method measurements, although more erratically for WA samples. Note that the lower values of OM density compared with AP density are because the optical images analyzed were taken in the center which does not account for the high density surface at the edge of the samples.
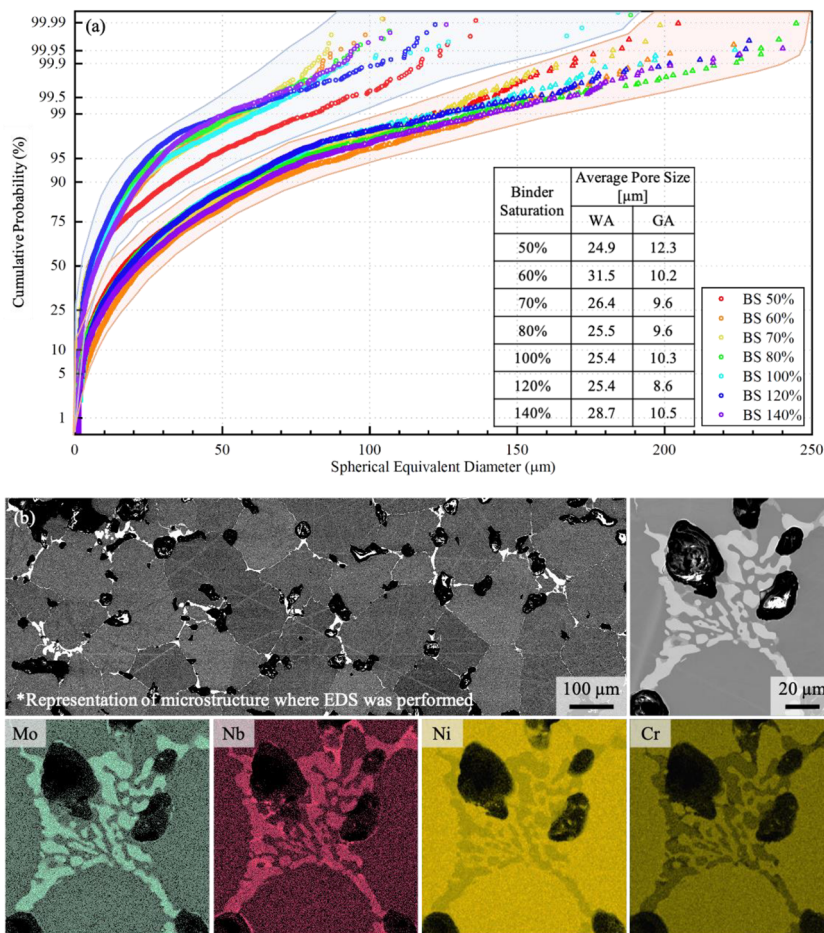
3.4 Porosity and microstructure analysis

Optical micrographs with visible details of pore shape and size were taken on the cross-sections of each sintered sample made from the two powder types and seven binder saturation levels and analyzed with ImageJ for pore size evolution. Figure 8a shows the cumulative probability plot of spherical equivalent pore size distribution with average pore size given in the table.

A comparison of the pores in the GA and WA sintered samples shows distinct distributions, enclosed by blue region and orange region for GA and WA, respectively. Samples printed with the same powder type show similar pore size distribution, except the GA samples with 50% binder saturations deviating somewhat from the other saturation levels. But, the median value of pores in GA samples is less than half of the median value in WA samples, and the pore distributions of WA samples move to the right as a whole on the probability plot. These differences clearly show the pore volume fraction in WA samples is significantly larger than in GA samples, consistent with previous reported results [1] and the current results in Fig. 7, which shows that the sintered density of WA samples is generally about 6% less than GA samples.

Figure 8b shows SEM micrographs and chemical analysis of elemental segregation at grain boundaries of sintered WA sample printed with 140% binder. A large number of pores, mostly irregularly shaped, were observed along grain boundaries. Small amounts of pores also exist inside grains. Based on the powder cross-section micrographs in Fig. 3a, b and the relatively low powder packing density in Fig. 4, there are two sources for pores in the final sintered microstructure: (1) pores are transferred from pre-existing pores in the powder [29]; (2)

Fig. 8 Porosity and elemental analysis of the sintered IN625 structure (a) cumulative probability plot of the pore size distribution from various sintered IN625 structure acquired from optical micrographs and ImageJ analysis. (b) BSE mode SEM micrograph and EDS elemental mappings of the cross-sections of sintered BJP WA IN625 alloy with 140% binder saturation

Binder Saturation	Average Pore Size [μm]	
	WA	GA
50%	24.9	12.3
60%	31.5	10.2
70%	26.4	9.6
80%	25.5	9.6
100%	25.4	10.3
120%	25.4	8.6
140%	28.7	10.5

voids form inevitably during powder packing process between particles. As these pores within and between powder particles cannot be fully eliminated during sintering step, pores are left in the sintered samples, with significant amounts in WA samples. High magnification micrographs (Fig. 8b) show bright precipitates along the grain boundaries for WA (Fig. 8b) and in a much smaller portion in GA samples (Supplemental Fig. 13). Since the solidus temperature for WA and GA IN625 powder is 1253 °C and 1283 °C respectively, sintering at 1270 °C for WA samples and 1285 °C for GA samples leads to higher extent of elemental segregation in WA microstructure, as shown in Supplemental Fig. 13. Energy-dispersive X-ray spectroscopy (EDS) maps, as shown in Fig. 8b, reveal the segregation region is enriched in Mo and Nb, and deprived of Ni and Cr. This enrichment of Nb could lead to the early formation of δ phase during post-build heat treatment [30].

3.5 Microhardness test

Like density, the microhardness (Fig. 9) is of considerable importance and is a good indication of bulk mechanical properties of sintered components. Microhardness of sintered WA samples showed an increase from 190 ± 9 to 206 ± 11 $HV_{0.1}$ with increasing binder saturation (50 to 70%) and then decrease to 179 ± 19 $HV_{0.1}$ upon further binder saturation increase. A similar pattern of hardness decreasing after increasing was observed in GA samples. For GA samples, hardness increased with increasing binder saturation to 223 ± 8 $HV_{0.1}$ up to 80% binder saturation. The highest microhardness values for WA and GA samples are reached at 70% and 80% binder saturations, respectively. It can be seen that for both WA and GA samples, the trends in microhardness, green density, and density after sintering depending on binder saturation levels agree almost exactly. This is because the indentation hardness of a sintered sample depends strongly on the density as voids in the structure of a part do not contribute to the support of the indenter.
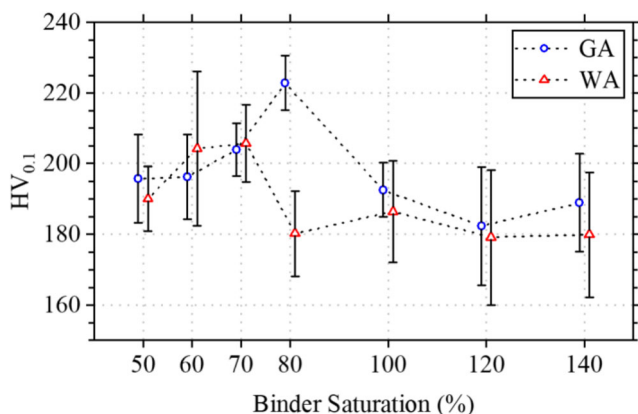

Fig. 9 Vickers microhardness values of the sintered WA and GA Inconel 625 samples printed at different binder saturation levels

Therefore, we can find that for GA samples increasing saturation levels up 80%, and for WA samples up to 70% resulted in a higher volume of binder during the printing process which subsequently improves bonding between power particles and lowers the pore volume fraction during sintering process. However, when binder saturation levels go beyond 80% for GA or 70% for WA, the volume occupied by the liquid binder is too large so that bonding becomes weak after the curing step and pores cannot be closed as much resulting in reduced sintered density and mechanical properties. Combing all the above results, 80% binder saturation is recommended for GA powder system, whereas 60 to 70% binder saturation is recommended for WA powder system.

## 3.6 Mechanism for binder bleeding and pore evolution

In light of the complexity of the BJP AM process, it is necessary to develop a fundamental understanding of powder-binder interaction and pore formation. For this purpose, we consolidated the current results of various binder-saturated Inconel 625 samples manufactured from GA and WA powders and the previously reported results in literature [10, 12, 16, 20, 21, 31, 32]. The following models of binder bleeding phenomenon during printing (Fig. 10) and pore evolution during printing and sintering processes (Fig. 11) are proposed.

Within this study, it was found that the particle morphology (sphericity and roundness) significantly influenced the powder-binder interaction. As stated by our results in Fig. 6 and Supplemental Fig. 12, the threshold where the binder bleeding phenomenon occurs is at a higher saturation level for GA powder (140%) than that for WA powder (120%). As shown in Figs. 4 and 10, changing the particle morphology altered the powder packing density and macro-void (pores) distribution within the powder bed, which subsequently influences the binder imbibition and drainage behaviors and the air gap distribution. In the BJP AM process, the deposited liquid binder takes over the place of the less viscous air, and migrates, via capillary pressure, into the macro-voids that are in the packed powder bed. The equilibrium condition is reached when capillary pressure across the binder-air interfaces is balanced out [12]. Under high binder saturation levels, two possible mechanisms of binder droplet dynamics within the powder bed might be responsible for the lower feature sharpness and binder bleeding phenomenon.

The first mechanism, the capillary pressure, which acts as the driving force for the binder migrating into the powder bed, varies in WA system and GA system. The capillary pressure in a powder bed system can be predicted based on the following Eq. 1 [20]:

$$P = \frac{S(1-\varepsilon)\gamma\cos\theta}{\varepsilon} \tag{1}$$

Fig. 10 Schematic diagram showing the mechanisms of the binder bleeding phenomenon in the powder bed of (a) spherical GA powder and (b) irregular WA powder. Layer n is the current layer, and layer n-1 is the one printed before layer n. Red arrows indicate the excessive binder migrates in the previously printed layers and lateral unsaturated areas; black arrows indicate the binder dragging the powder down which promotes the densification of the n-1 layer
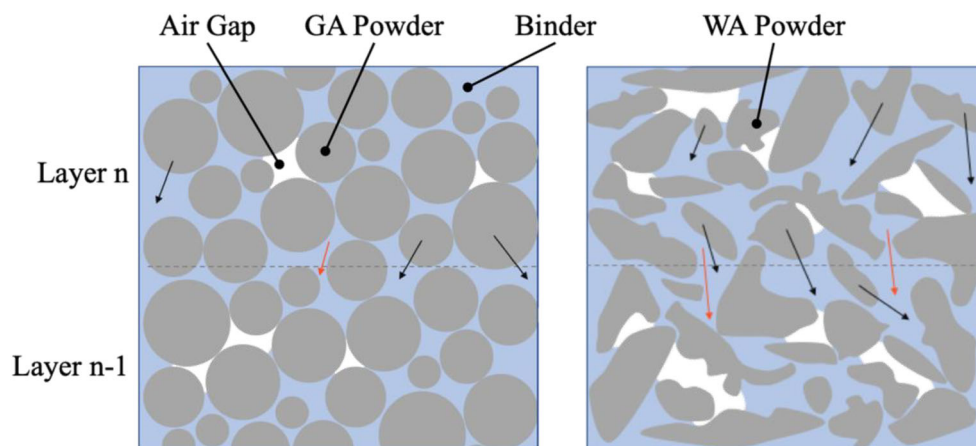
where P is the capillary pressure between the binder droplet and the powder particles, S is the specific surface area (surface area/volume) of the powder bed, θ is the contact angle of the binder fluid with the powder particle, ε is the porosity of the powder bed, and γ is the surface tension of the liquid binder. It is clear that the specific surfaces and packing densities are the most important factors affecting capillary pressure. An increase in packing density brings a reduction in macro-voids in the powder bed, which corresponds to a higher capillary pressure and more uniformly wetted porous structure. Therefore, when the same amount of binder is deposited to WA and GA powder bed, a larger portion of air gaps (denoted as white areas in Fig. 10) is retained in the powder bed of irregular WA powder, which in fact lowers the actual binder saturation compared with that in GA system. The unrestricted binder that is not able to fill in the macro-voids in the WA

powder bed migrates both laterally and vertically to the surrounding unsaturated area which causes the bleeding phenomenon visible at a lower saturation level than that in the GA case.

The second mechanism that is crucial with regard to powder-binder interaction is the drying of the binder. As the deposited binder volume increases with increasing binder saturation levels, the same drying time may not be enough to sufficiently dry the binder in each layer compared to layers printed with a lower amount of binder. As a result, high saturations promote the continued binder penetration and spreading and reduce stability introduced during compaction of the previous layers. As illustrated in Fig. 10, binder deposited on the current layer (n) may seep into the previous layer and pull powder particles to air gaps or locations unoccupied by powder of the previous layer (n-
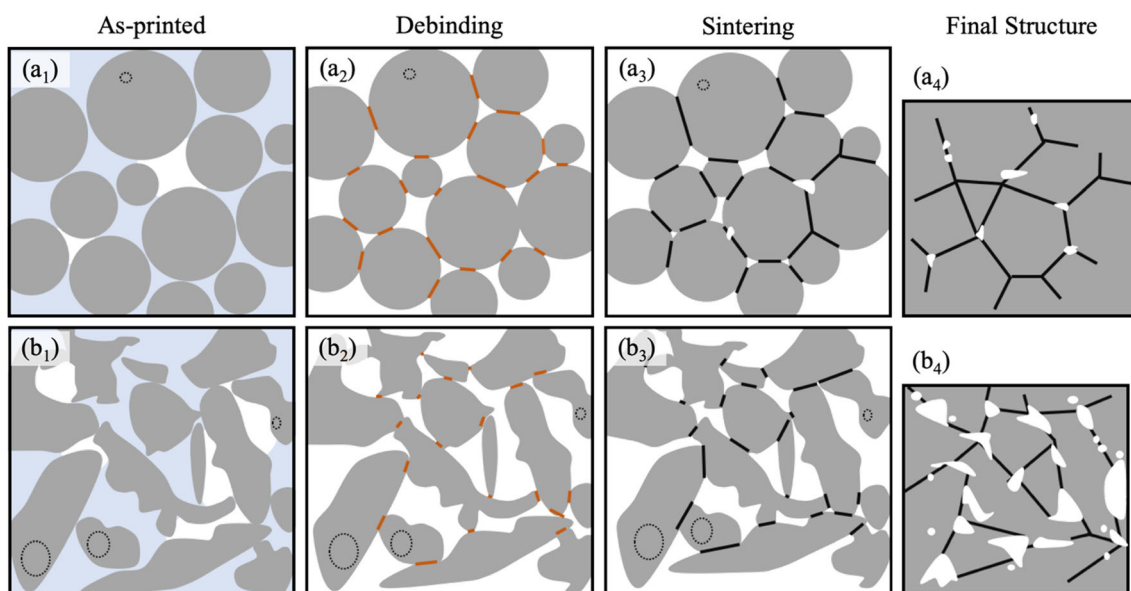

Fig. 11 Schematic illustration showing the general process in two dimensions for a binder jet printing system of (a) spherical powder and (b) irregular powder: (a_1,b_1) as-printed powders, (a_2,b_2) debound powders which are bonded by pendular bonds, (a_3,b_3) powders as they begin to adopt the shape of a polyhedron in three dimensions and to enclose the pore channels at the grain boundaries during sintering, and (a_4,b_4) enclosed pores at the corners where polyhedrons meet present in the final sintered structure

1). This may lead to more inaccurate part dimensions due to poor binder penetration and spreading. As there is a greater proportion of air gaps preserved in the WA system due to powder morphology, this binder and particle migration becomes more evident. For lower binder saturations, these phenomena are less perceptible.

Figure 11 compares the pore evolution in WA and GA powder bed during printing and sintering process. In the curing process, the water evaporates from the water-based binder, and pendular bonds (indicated by orange bars in Fig. 11a$_2$,b$_2$) are left to hold the powder particles together. The SEM micrographs of the cured green parts at 140% binder saturation in Supplemental figure 14b,c clearly show the pendular bonds in WA and GA samples. To achieve Inconel components with satisfactory mechanical properties, the green part densification must be completed by sintering. The sintered density of the final part is closely related to its mechanical properties. Through a diffusion process and driven by the reduction of the surface area of a system, powder particles are coalesced by metallic bonds in the sintering process. The change in sintering process is illustrated in Fig. 11a$_3$,b$_3$, where powder particles are coalesced by sintering necks (indicated by black bars) and have begun to adopt the shape of a polyhedron in three dimensions. Grain boundaries continue to lengthen and move to accommodate further grain growth and pore removal. Pores become angular and subsequently pinch off and become isolated along the grain edge. This results in substantial densification and shrinkage which is equivalent to the amount of porosity reduction. At the final stage in Fig. 11a$_4$,b$_4$, pores are eliminated to a large extent at the expense of dimensional shrinkage, and the part will have its maximum density, giving mechanical strength to the final parts. The shrinkage of GA sample is less than WA samples, which is represented as the difference in the area of Fig. 11a$_4$,b$_4$, due to higher green density of the GA samples and larger contact area which facilitates the diffusion process during sintering. As shown in Supplemental figure 13, in GA samples, the pores are small in size and located almost exclusively on the grain boundaries. However, as mentioned earlier, a larger amount of porosity along the grain boundaries and within grains is kept in final sintered WA structure. These pores might come from the inability to fully close the macro-voids in the powder bed and the internal pores from the powder particles (indicated as dashed black circles in Fig. 11a$_1$-a$_3$,b$_1$-b$_3$).

The difficulty in sintering WA IN625 samples prepared by BJP AM technique is not surprising given the inferior packing density of the particles. The characteristics of WA powder create a large portion of inter-particle macro-voids within the powder which lowers WA powder packing density and the densification during the sintering process due to larger contact spacing and lower contact area which increases diffusion path length and, therefore, slows diffusion in WA powder samples.

4 Conclusion

This detailed study about the effect of binder saturation levels and powder morphology on green density, dimensional accuracy, sintered density, microhardness, and binder bleeding phenomenon, draws the following conclusions:

1. The printed powder packing density of WA and GA Inconel 625 powder is measured to be 46% and 58% due to the variation in particle sphericity and roundness. For both powder systems, increasing binder saturation increased the green density, sintered density, and microhardness, and then a plateau was reached. Further increasing binder saturation causes not only degradation in green density and microhardness but also generates a binder bleeding phenomenon and poor dimensional accuracy.
2. The optimal binder saturation levels for WA and GA powder systems with the present particle size distributions are determined to be 60–70%, and around 80%, respectively. Under the optimal saturation level, optimal sintered density and microhardness can be achieved. For WA samples, the sintered density and hardness values are 90% and 206 HV$_{0.1}$, respectively; for GA samples, these two values are >99% and 223 HV$_{0.1}$.
3. The critical thresholds of binder saturation for WA and GA systems at which excessing binder bleeding occurs are determined to be 120% and 140%. The mechanism for the lower binder tolerance in WA systems is attributed to the larger portion of air gap that exists in the WA powder bed caused by lower capillary pressure between the WA powder particles and binder fluid.
4. Phase and porosity evolution of WA and GA samples were very different. A large number of pores along the grain boundaries and inside the grains were observed in WA samples, whereas only a small amount of pores along the grain boundary are found in GA microstructure. Elemental segregation of Nb and Mo accumulated around the pore and grain boundaries forms at WA samples, while very little extent of segregation occurred in GA samples.

Declarations

Conflicts of interest The authors declare no competing interests.

References

1. Mostafaei A, Toman J, Stevens EL, Hughes ET, Krimer YL, Chmielus M (2017) Acta Materialia Microstructural evolution and mechanical properties of differently heat-treated binder jet printed samples from gas- and water-atomized alloy 625 powders. Acta Mater 124:280–289. https://doi.org/10.1016/j.actamat.2016.11.021

2. Chyrkin A, Bo C, Barnikel J, Schmitz F, Quadakkers WJ (2014) Oxidation behaviour and microstructural stability of alloy 625 during long-term exposure in steam:6127–6142. https://doi.org/10.1007/s10853-014-8344-7

3. Mostafaei A, Behnamian Y, Krimer YL, Stevens EL, Li J, Chmielus M (2016) Effect of solutionizing and aging on the microstructure and mechanical properties of powder bed binder jet printed nickel-based superalloy 625. JMADE. 111:482–491. https://doi.org/10.1016/j.matdes.2016.08.083

4. Nandwana P, Elliott AM, Siddel D, Merriman A, Peter WH, Babu SS (2017) Powder bed binder jet 3D printing of Inconel 718 : densification , microstructural evolution and challenges q. Curr Opin Solid State Mater Sci 21:207–218. https://doi.org/10.1016/j.cossms.2016.12.002

5. Cunningham R, Nicolas A, Madsen J, Fodran E, Sangid MD, Rollett AD (2017) Analyzing the effects of powder and post- processing on porosity and properties of electron beam melted Ti-6Al-4V. Mater Res Lett 5:1–10. https://doi.org/10.1080/21663831.2017.1340911

6. Jiang R, Mostafaei A, Pauza J, Kantzos C, Rollett AD (2019) Varied heat treatments and properties of laser powder bed printed Inconel 718. Mater Sci Eng A 755:170–180. https://doi.org/10.1016/j.msea.2019.03.103

7. Spierings AB, Voegtlin M, Bauer T, Wegener K (2016) Powder flowability characterisation methodology for powder-bed-based metal additive manufacturing. Prog Addit Manuf 1:9–20. https://doi.org/10.1007/s40964-015-0001-4

8. Vlasea M, Toyserkani E, Pilliar R (2015) Effect of gray scale binder levels on additive manufacturing of porous scaffolds with heterogeneous properties. 70:62–70. https://doi.org/10.1111/ijac.12316

9. Pontevedra V, Santana A, Afonso P, Zanin A, Wernke R (2018) ScienceDirect ScienceDirect ScienceDirect Influence of Binder Quantity on Dimensional Accuracy and Influence of Binder Quantity on Dimensional Accuracy and in 3D-Printing Manufacturing Engineering Resilience Resilience in 3D-Printing Costing models for ca. Procedia Manuf 21:638–646. https://doi.org/10.1016/j.promfg.2018.02.166

10. Lv X, Ye F, Cheng L, Fan S, Liu Y (2019) Binder jetting of ceramics : powders , binders , printing parameters , equipment , and post-treatment. Ceram Int 45:12609. https://doi.org/10.1016/j.ceramint.2019.04.012

11. Espalin D, Macdonald E, Wicker RB (2015) Author ' s Accepted Manuscript. Ceram Int 41:6610–6619. https://doi.org/10.1016/j.ceramint.2015.01.108

12. Miyanaji H, Yang L (2016) Equilibrium saturation in binder jetting additive manufacturing processes: theoretical model vs. experimental observations. International Solid Freeform Fabrication Symposium, Austin, TX, pp 1945–1959

13. Xia M, Nematollahi B, Sanjayan J (2018) Influence of binder saturation level on compressive strength and dimensional accuracy of powder-based 3D printed geopolymer influence of binder saturation level on compressive strength and dimensional accuracy of powder-based 3D printed geopolymer. https://doi.org/10.4028/www.scientific.net/MSF.939.177.

14. Materials H, Enneti RK, Prough KC (2019) International Journal of Refractory Metals E ff ect of binder saturation and powder layer thickness on the green strength of the binder jet 3D printing (BJ3DP) WC-12 % Co powders. Int J Refract Met Hard Mater 84:104991. https://doi.org/10.1016/j.ijrmhm.2019.104991

15. Li S, Cao S (2012) Print parameters influence on parts ' quality and calibration with 3DP- Part II : Print parameters calibration and contour accuracy control. 401:1687–1692. https://doi.org/10.4028/www.scientific.net/AMR.399-401.1687

16. Castilho M, Gouveia B, Pires I, Rodrigues J, Pereira M, Pereira M (2015) The role of shell / core saturation level on the accuracy and mechanical characteristics of porous calcium phosphate models produced by 3Dprinting. https://doi.org/10.1108/RPJ-02-2013-0015

17. Vaezi M, Chua CK (2014) Effects of layer thickness and binder saturation level parameters on 3D printing process. https://doi.org/10.1007/s00170-010-2821-1

18. Nandwana P, Elliott AM, Siddel D, Merriman A, Peter WH, Babu SS (2017) Powder bed binder jet 3D printing of Inconel 718: Densification, microstructural evolution and challenges☆. Curr Opin Solid State Mater Sci 21:207–218. https://doi.org/10.1016/j.cossms.2016.12.002

19. Caputo M, Solomon CV, Nguyen P, Berkowitz AE (2019) Electron microscopy investigation of binder saturation and microstructural defects in functional parts made by additive manufacturing. 22: 1770–1771. https://doi.org/10.1017/S1431927616009697

20. Miyanaji H, Zhang S, Yang L (2018) International Journal of Machine Tools and Manufacture A new physics-based model for equilibrium saturation determination in binder jetting additive manufacturing process. Int J Mach Tools Manuf 124:1–11. https://doi.org/10.1016/j.ijmachtools.2017.09.001

21. Miyanaji H, Orth M, Akbar JM et al (2018) Process development for green part printing using binder jetting additive manufacturing. Front Mech Eng 13:504–512. https://doi.org/10.1007/s11465-018-0508-8

22. Bredt J (1995) Binder stability and powder/binder interaction in three dimensional printing. Thesis (Ph. D.) - Massachusetts Institute of Technology, Dept. of Mechanical Engineering. http://hdl.handle.net/1721.1/10999. Accessed 20 April 2021

23. Schneider CA, Rasband WS, Eliceiri KW (2012) NIH Image to ImageJ: 25 years of image analysis. Nat Methods 9:671–675. https://doi.org/10.1038/nmeth.2089

24. Oh J, Nahm S, Kim B, Choi H (2019) Anisotropy in green body bending strength due to additive direction in the binder-jetting

additive manufacturing process. 57:227–235. https://doi.org/10.3365/KJMM.2019.57.4.227

25. Cunningham R, Nicolas A, Madsen J, Fodran E, Anagnostou E, Sangid MD, Rollett AD (2017) Analyzing the effects of powder and post-processing on porosity and properties of electron beam melted Ti-6Al-4V. Mater Res Lett 5:516–525. https://doi.org/10.1080/21663831.2017.1340911

26. Mostafaei A, Hilla C, Stevens EL, Nandwana P, Elliott AM, Chmielus M (2018) Comparison of characterization methods for differently atomized nickel-based alloy 625 powders. Powder Technol 333:180–192. https://doi.org/10.1016/j.powtec.2018.04.014

27. Alshibli KA, Druckrey AM, Al-Raoush RI, Weiskittel T, Lavrik NV (2014) Quantifying morphology of sands using 3D imaging. J Mater Civ Eng 27:04014275. https://doi.org/10.1061/(asce)mt.1943-5533.0001246

28. Brika SE, Letenneur M, Dion CA, Brailovski V (2019) Influence of particle morphology and size distribution on the powder flowability and laser powder bed fusion manufacturability of Ti-6Al-4V alloy. Addit Manuf 31:100929. https://doi.org/10.1016/J.ADDMA.2019.100929

29. German RM (2010) Liquid phase sintering. In: Thermodynamics of sintering. Woodhead Publishing Limited. https://doi.org/10.1533/9781845699949.1.110

30. Kantzos C, Pauza J, Cunningham R, Narra SP, Beuth J, Rollett A (2018) An investigation of process parameter modifications on additively manufactured Inconel 718 parts. J Mater Eng Perform 28:620. https://doi.org/10.1007/s11665-018-3612-3

31. Marmur A (1988) Penetration of a small drop into a capillary. J Colloid Interface Sci 122:209–219. https://doi.org/10.1016/0021-9797(88)90304-9

32. Zhou Z, Buchanan F, Mitchell C, Dunne N (2014) Printability of calcium phosphate : calcium sulfate powders for the application of tissue engineered bone scaffolds using the 3D printing technique. Mater Sci Eng C 38:1–10. https://doi.org/10.1016/j.msec.2014.01.027